Discharging shape influence on the performance of a latent heat thermal energy storage

Cite as: AIP Conference Proceedings **2191**, 020079 (2019); https://doi.org/10.1063/1.5138812
Published Online: 17 December 2019

Francesco Fornarelli, Marco Torresi, Paolo Oresta, Lorenzo Dambrosio, Adio Miliozzi, and Sergio Mario Camporeale

Discharging shape influence on the performance of a latent heat thermal energy storage

Francesco Fornarelli[1,a)], Marco Torresi[1], Paolo Oresta[1], Lorenzo Dambrosio[1], Adio Miliozzi[2] and Sergio Mario Camporeale[1]

[1]*Dipartimento di Meccanica, Matematica e Management. Politecnico di Bari, Italy.*
[2]*ENEA – Italian National Agency for New Technologies, Energy and Sustainable Economic Development, Casaccia Research Centre, Italy.*

[a)]Corresponding author: francesco.fornarelli@poliba.it

Abstract.
Due to the mismatching between the renewable energy source and the energy demand, the energy storage devices have attracted the attention of the scientific community in order to maximize their performance. Several technologies have been developed and applied in laboratory scale and prototypes in the last decades. The energy storage devices can be mainly defined according to the average working temperature, the storage material, and the geometrical configuration. This work is focused on the 2D axisymmetric finite volume multiphase numerical simulations of the fluid flow and heat transfer within a shell-and-tube type latent heat thermal energy storage (LHTES). The effect of the geometrical parameters on the thermal performance of such systems is investigated. The influence of the LHTES shape is highlighted keeping constant the heat exchange area, the total storable heat and the heated surface temperature. Detailed description of the liquid fraction and temperature distribution during the solidification phase are reported. The solidification phase appears strongly influenced by the geometry. The geometries have been chosen according to fixed volume and heat exchange area condition. The ratio between the external and the internal radius (r_e/r_i) has been changed and its effect on the thermal performance of the thermal storage device is considered. Thus, according to the application requirement, particular care should be taken in the design of the shape of the LHTES device.

INTRODUCTION

The low carbon energy production systems represent a key point in order to reach the main objective to reduce the CO_2 concentration in the next decades. On the other hand, the renewable energy systems are affected by unpredictable availability that is mostly uncorrelated with the energy demand. Therefore, the development of heterogeneous power systems that use different energy sources, connected with each other, represents a key point in the scientific community. Starting from the single device optimization, to the control of complex systems several scientific field are involved [1, 2]. In this scenario, the energy storage can increase the efficiency of renewable energy in the power grid [3]. The energy storage includes batteries, chemical reactions and thermal storage, to cite a few. In the last years, the thermal energy storage represented an interesting option in the integration of Concentrated Solar Plant (CSP) in the energy production power grid [4, 5]. The thermal energy storage applications include several types due to the storing materials, device configuration and the physical behavior of the storing materials. The thermal storage systems consist in a Heat Transfer Fluid (HTF) that is able to transfer the heat from the solar receiver to the heat storage. In order to maximize the stored heat per unit mass, the storage is typically made of high capacity materials. However, the heat transfer rate represents a bottle neck in the design of such a system. Thus, the promotion of the heat transfer within the storage represents a key feature that engineers and scientists investigate in the last decades [6, 7, 8, 9, 10]. Indeed, the increase of the area-volume ratio by means of finned surfaces gives an improvement of the heat transfer rate. This approach fits the application with solid materials (i.e. concrete, sand) that involves conductive heat transfer. In order to increase the heat storage capacity per unit mass, phase change materials (PCMs) can be considered [11, 12]. According to the temperature range, the PCMs considered are able to melt and to solidify during the excess and depletion of heat production from the heat source, respectively. The liquid phase is able to induce convective motions and then

74th ATI National Congress
AIP Conf. Proc. 2191, 020079-1–020079-10; https://doi.org/10.1063/1.5138812
Published by AIP Publishing. 978-0-7354-1938-4/$30.00

to increase the heat transfer within the PCM. The promotion of heat transfer, with respect to a pure conductive case, is investigated by several works both numerical and experimental, where the main contribution appears during the melting phase [13, 14, 15, 16, 17]. Indeed, during the melting the hot wall is next to the melted PCM that is able to buoyant and trig the convective motions. On the other hand, the solidification phase takes more time according to the solidification along the cold wall boundary of the PCM. The solid PCM layer at the heat exchange wall dump the temperature at the interface between solid and liquid PCM lowering the buoyant effect that influence the convection [18]. Thus, the effect of geometrical parameters of a shell-and-tube LHTES device on its discharging (solidification) performance is here investigated. Four different geometrical configurations have been taken into account keeping constant the overall storage volume, the heat exchange area and the heated wall temperature. The results are also compared with the charging phase results discussed in a Fornarelli et al. [19].

Problem outline

The geometry here considered is a well-known shell-and-tubes configuration that could be approximated by means of a single module configuration. The device has an internal duct, where the HTF flows, imposing a flow rate and an inlet temperature and an external closed coaxial shell filled with the storage material. The device is usually vertically placed in order to promote the buoyancy effect. In figure 1, a schematic of the problem is presented. The main geometry parameters are then the internal and external radius of the PCM enclosure and its height. The details of the geometrical parameters for each case are reported in table 1. In each case, the volume has been kept constant ($V = 1.82 \cdot 10^{-3} m^3$) in order to do not change the overall thermal capacity of the thermal storage and the internal heat exchange area is kept constant too ($A = 2.51 \cdot 10^{-2} m^2$). The temperature change of the HTF along the height is neglected according to the previous experimental investigation [20]. They highlight, for certain values of the HTF flow rate and for geometrical configurations similar to those here studied, the temperature difference of the HTF, between the inlet and the outlet, is within few degrees. Thus, the HTF can be avoided to be numerically solved and a constant boundary condition for the temperature at the heat exchange wall can be considered, $T_{wall} = 473K$. The comparison between different geometries are still valid and this work is able to give a feedback to the effects of the geometries on the thermal response of the system.

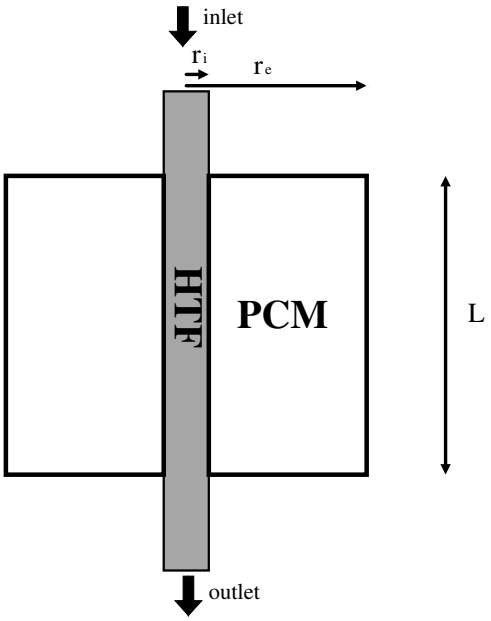

FIGURE 1. Schematic of a single module of the shell-and-tube LHTES device. The main geometrical characteristics are reported.

The PCM is considered to be a binary mixture of sodium and potassium salts ($NaNO_3 60\%wt - KNO_3 40\%wt$) whose main physical characteristics are reported in table 2.

TABLE 1. Main geometrical characteristics of the test cases.

	test 1	test 2	test 3	test 4
r_e/r_i	2	3	4.375	6
$r_e\,[mm]$	97	54	35	25
$r_i\,[mm]$	48	18	8	4
$L\,[mm]$	83	221	500	965
$V/A\,[1/m]$	0.0725	0.0725	0.0725	0.0725
$r_e - r_i$	49	36	27	21
$L/(r_e - r_i)$	1.69	6.1	18.5	45.9

TABLE 2. Physical properties of the PCM. T is in K.

Properties	Values	
Density	$\rho_{PCM} = 1994$	$\left(\frac{kg}{m^3}\right)$
Thermal Expansion Coefficient	$\beta_{PCM} = 3.18861 \cdot 10^{-4}$	$\left(\frac{1}{K}\right)$
Specific Heat	$c_{p,PCM} = 1626$	$\left(\frac{J}{kg \cdot K}\right)$
Conductivity	$k_{PCM} = 0.4886$	$\left(\frac{W}{m \cdot K}\right)$
Dynamic Viscosity	$\mu_{PCM} = 7.008 \cdot 10^{-3}$	$\left(\frac{kg}{m \cdot s}\right)$
Solidus Temperature	$T_{sol} = 493.03$	(K)
Liquidus Temperature	$T_{liq} = 517.29$	(K)
Latent Heat	$\Lambda = 1.10 \cdot 10^5$	$\left(\frac{J}{kg}\right)$

Numerical Model

The governing equations for the PCM include the continuity, momentum and energy. The Boussinesq approximation is considered in order to couple the momentum and energy equation. The solid/liquid phase change is modelled with a penalty approach adding a fictitious friction term on the right hand side of the momentum equations. The model is described in details in the literature [21, 22, 23, 24, 25, 26, 27], and implemented in Ansys Fluent, a commercial CFD software. Here follows the detailed governing equations:

$$\nabla \cdot \bar{u} = 0 \tag{1}$$

$$\rho\left(\frac{\partial \bar{u}}{\partial t} + \bar{u}\nabla\bar{u}\right) = -\nabla p + \rho'\bar{g} + \bar{S} + \nabla \cdot \bar{\bar{\tau}} \tag{2}$$

$$\rho\frac{\partial(H)}{\partial t} + \rho\nabla(H\bar{u}) = \nabla(k\nabla T). \tag{3}$$

where, $\bar{u}$ represents the velocity vector, t is the time, p the pressure scalar field, $\bar{g}$ the gravity acceleration and $\bar{\bar{\tau}}$ the viscous stress tensor. In the energy equation (eq. 3), H is the enthalpy, and k represents the thermal conductivity. In order to take into account the buoyancy effect, the Bousinnesq approximation is considered with $\rho' = \rho(1 - \alpha\Delta R)$, representing the modified density related to the average density of the PCM, ρ, the temperature change, ΔT, and the thermal expansion coefficient, α. The model includes a source term, S, that belongs from the *Carman-Kozeny* equation:

$$S = \frac{(1-\beta_l)^2}{(\beta_l^3 + \epsilon)} A_{mush}\vec{u} \tag{4}$$

It is also called a *penalty approach*, due to the added artificial viscous effect in the momentum equation when the liquid fraction, β_l, is less then 1. The A_{mush} is the mushy zone constant and it depends on the material, higher the A_{mush} is, higher the added viscous resistance will be. The term ϵ is a small number that prevents the singularity for

$\beta_l = 0$. According to previous works of the authors, the value of the A_{mush} is set to $10^5\ kg/(m^3 s)$. In the model, the liquid fraction, β_l, depends linearly on the temperature according to the following relations:

$$\beta_l = \begin{cases} 0 & \text{if } T < T_{sol} \\ \dfrac{T - T_{sol}}{T_{liq} - T_{sol}} & \text{if } T_{sol} < T < T_{liq} \\ 1 & \text{if } T > T_{liq} \end{cases} \tag{5}$$

In the range of the parameters setup, the problem is axisymmetric, hence a 2D axisymmetric condition is considered. The grid size has been chosen according to the sensitive analysis made in a previous work of the authors [19].

Results

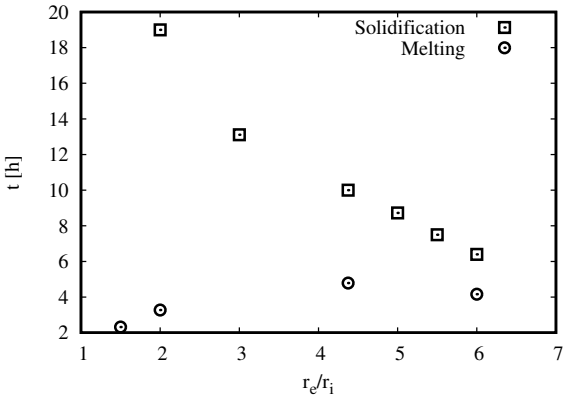

FIGURE 2. Overall solidification time (open square) with respect to the radii ratio, r_e/r_i. The overall melting time of the same geometries are reported. Details of the melting cases are reported in [19]

The CFD analysis has been performed over four different geometries, whose dimensional details are reported in table 1. The total volume and heat exchange area have been kept constant. The radii ratio between the external and internal radius of the PCM enclosure has been changed considering the following values: $r_e/r_i = 2,\ 3,\ 4.375$ and 6. The time of complete solidification with respect to the radii ratio are reported in figure 2. The solidification time

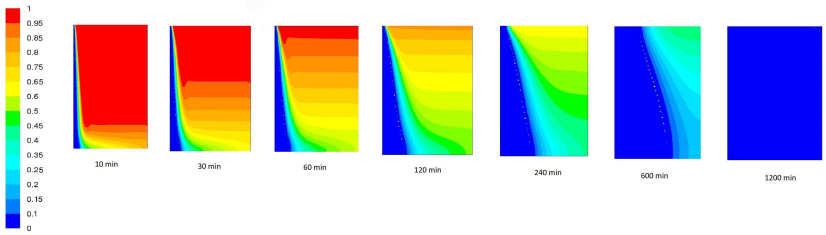

FIGURE 3. Contours of the liquid fraction during the solidification process for the case $r_e/r_i = 2$. The left side is the cold wall, where the temperature is kept constant at $473K$, below the solidification temperature of the PCM. The time from the beginning of the solidification cycle are reported.

decreases increasing the radii ratio from $r_e/r_i = 2$ to 4.375. Then, further increasing of the radii ratio, up to $r_e/r_i = 6$, does not imply an overall solidification time reduction, but a slight solidification time increment is recognized. It is worth noting that the corresponding melting time for the same geometries [19] has an opposite behavior, where

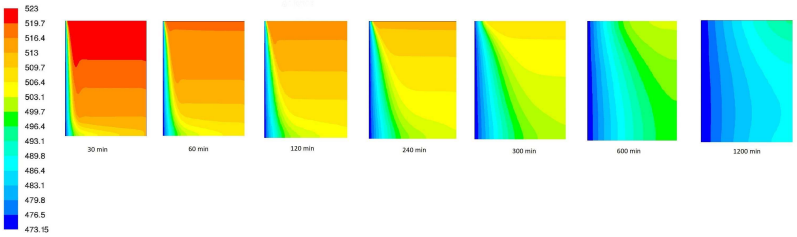

FIGURE 4. Contours of the temperature during the solidification process for the case $r_e/r_i = 2$. The left side is the cold wall, where the temperature is kept constant at $473K$, below the solidification temperature of the PCM. The time from the beginning of the solidification cycle are reported.

the melting time increases from $r_e/r_i = 1.5$ to 4.375 and then it reduces for $r_e/r_i = 6$. Moreover, the solidification phase is stiffer than the melting one. Indeed, the convective effect during the melting phase are higher than that in the solidification time. This result has been also remarked in [15, 18] for the geometry $r_e/r_i = 4.375$ with different boundary condition and a more complicated model considering even the HTF fluid flow and heat exchange in the numerical model. The geometry with $r_e/r_i = 2$ has a smallest aspect ratio $L/(r_e - r_i) = 1.69$ of the shell-and-tube

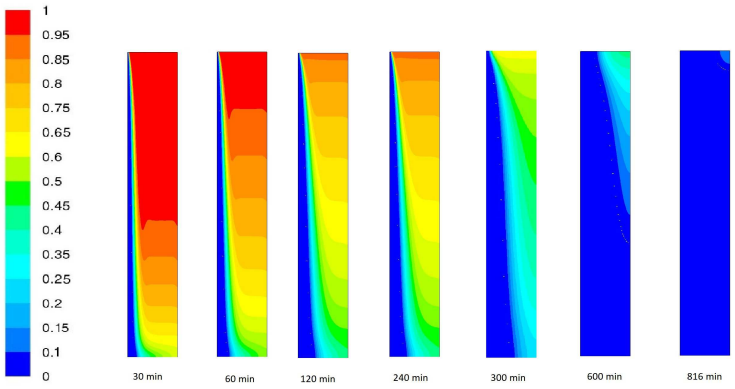

FIGURE 5. Contours of the liquid fraction during the solidification process for the case $r_e/r_i = 3$. The left side is the cold wall, where the temperature is kept constant at $473K$, below the solidification temperature of the PCM. The time from the beginning of the solidification cycle are reported.

module and the highest thickness of the PCM $r_e - r_i = 49$ with respect the other cases. In figure 3 and figure 4 the liquid fraction and the temperature spatial distribution during the solidification process is reported. The solidification process lasts about $17h$ to be completed. The solidification is not homogeneous during the whole process, but a vertical stratification of the hot and cold salts is well described by the liquid fraction and temperature distribution. Hence, the upper part of the PCM is the last that solidifies.

The $r_e/r_i = 3$ (figures 5 and 6) and $r_e/r_i = 4.375$ (figures 7 and 8) speed up the solidification process according to the height, L, increasing and the reduction of the thickness, $r_e - r_i$, of the PCM. The conduction is dominant with respect to the convection, however, the stratification of the PCM within the enclosure remarks that a convective effect exist that moves the hot PCM toward the upper part and push the cold one in the bottom. The improvement of the PCM performance in terms of solidification time reduction, reaches an optimal condition at $r_e/r_i = 4.375$. At $r_e/r_i = 6$, the geometry appears very slender with respect to the other, and the convection of the PCM seems to be limited by the confinement of the material within the small thickness of PCM, $r_e - r_i = 21mm$. Then, the stratification of the PCM is no more efficient and the viscous effect of the walls becomes dominant (figures 9 and 10).

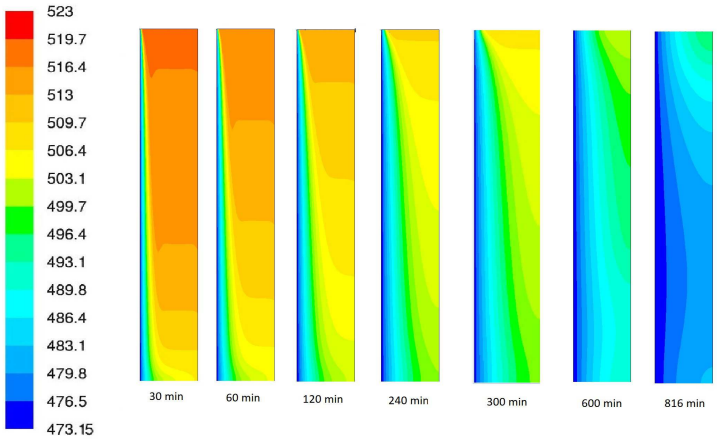

FIGURE 6. Contours of the temperature during the solidification process for the case $r_e/r_i = 3$. The left side is the cold wall, where the temperature is kept constant at $473K$, below the solidification temperature of the PCM. The time from the beginning of the solidification cycle are reported.

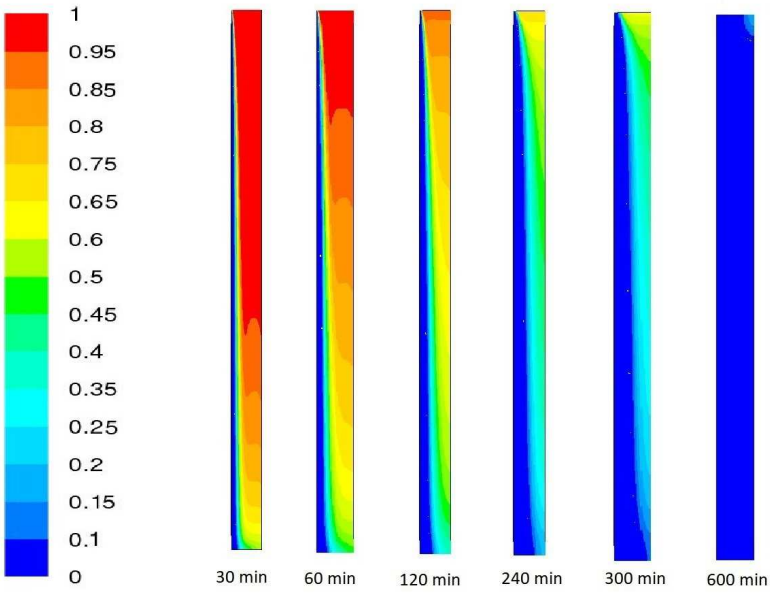

FIGURE 7. Contours of the liquid fraction during the solidification process for the case $r_e/r_i = 4.375$. The left side is the cold wall, where the temperature is kept constant at $473K$, below the solidification temperature of the PCM. The time from the beginning of the solidification cycle are reported.

Conclusions

The work shows numerical simulation results of a shell-and-tube LHTES device in several geometrical configurations. The geometrical constraints on the storage material volume, to keep the overall thermal energy storage constant, and

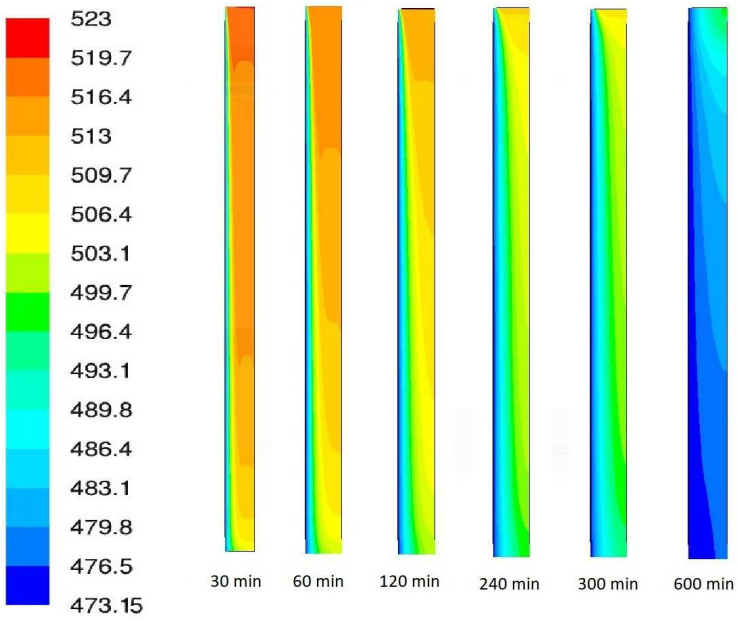

FIGURE 8. Contours of the temperature during the solidification process for the case $r_e/r_i = 4.375$. The left side is the cold wall, where the temperature is kept constant at $473K$, below the solidification temperature of the PCM. The time from the beginning of the solidification cycle are reported.

the heat exchange area of the internal lateral surface of the cylinder have been considered. The numerical results highlight that the liquid PCM stratifies with respect to the vertical direction due to the natural convection effect. Indeed, the hot PCM buoys with respect to the cold one. The comparison between the results shows that the solidification time has a minimum for the case with the radii ratio $r_e/r_i = 4.375$. The decreasing of the radii ratio up to $r_e/r_i = 2$ shows a sensible increasing of the overall solidification time according to the reduction in the buoyancy that is related to the height of the geometry, L. Further increasing of the re/ri from 4.375 to 6 does not influence positively the performance characteristic of the LHTES due to the geometrical constraints that affects the thickness of the PCM, $r_e - r_i$. The viscous effect in the narrow region becomes dominant, limiting the buoyancy effect of the convection. A comparison with previous results of the authors [19] remarks a competing effect of the geometry on the melting and solidification time that has to be taken into account in the design process of the LHTES device.

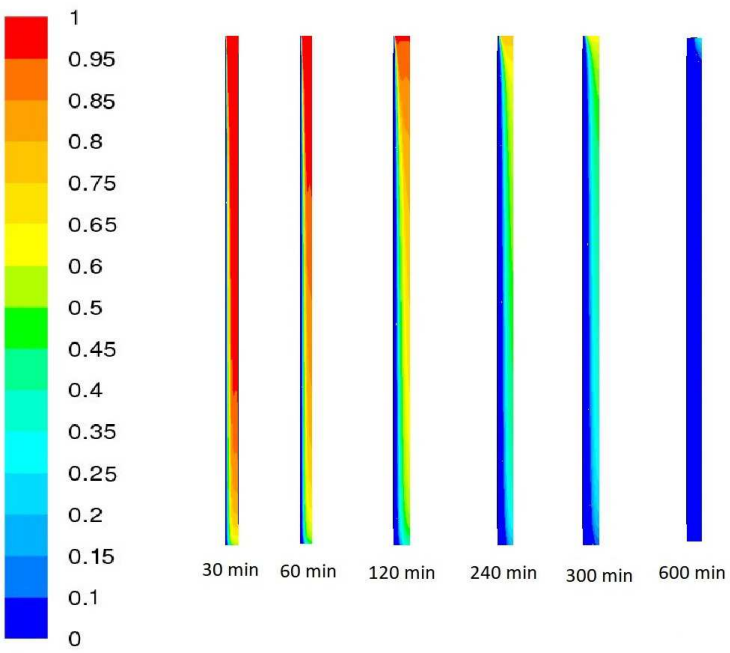

FIGURE 9. Contours of the liquid fraction during the solidification process for the case $r_e/r_i = 6$. The left side is the cold wall, where the temperature is kept constant at $473K$, below the solidification temperature of the PCM. The time from the beginning of the solidification cycle are reported.

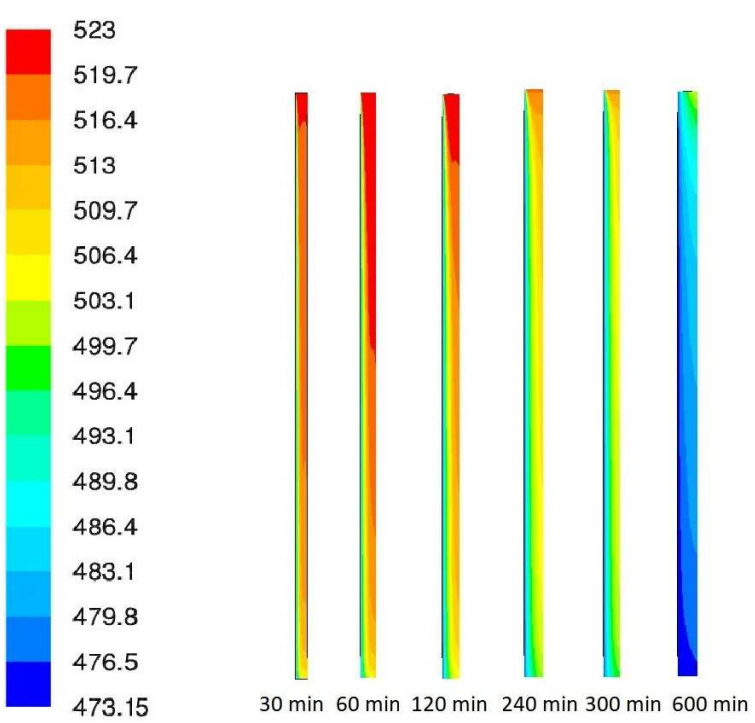

FIGURE 10. Contours of the temperature during the solidification process for the case $r_e/r_i = 6$. The left side is the cold wall, where the temperature is kept constant at $473K$, below the solidification temperature of the PCM. The time from the beginning of the solidification cycle are reported.

REFERENCES

[1] L. Dambrosio, 2018 5th International Conference on Control, Decision and Information Technologies, CoDIT 2018 98–103 (2018).

[2] L. Dambrosio, B. Fortunato, M. Torresi, S. Mario Camporeale, and F. Fornarelli, Energy Procedia **126**, 533–540 (2017).

[3] M. Short, T. Crosbie, M. Dawood, and N. Dawood, Applied Energy **186**, 304 – 320 (2017), sustainable Thermal Energy Management (SusTEM2015).

[4] E. Bufi, S. Camporeale, F. Fornarelli, B. Fortunato, A. Pantaleo, A. Sorrentino, and M. Torresi, Energy Procedia **126**, 429–436 (2017).

[5] B. Fortunato, S. Camporeale, M. Torresi, F. Fornarelli, G. Brunetti, and A. Marco Pantaleo, Proceedings of the ASME Turbo Expo **3** (2016), 10.1115/GT2016-58159.

[6] M. Chieruzzi, G. Cerritelli, A. Miliozzi, and J. Kenny, Nanoscale Research Letters **8** (2013), 10.1186/1556-276X-8-448.

[7] F. Fornarelli, P. Oresta, and A. Lippolis, JP Journal of Heat and Mass Transfer **11**, 1–28 (2015).

[8] F. Fornarelli, A. Lippolis, and P. Oresta, Journal of Heat Transfer **139** (2016), 10.1115/1.4034794.

[9] M. Liu, W. Saman, and F. Bruno, Renewable and Sustainable Energy Reviews **16**, 2118–2132 (2012).

[10] M. Torresi, A. Saponaro, S. Camporeale, and B. Fortunato, Proceedings of the ASME Turbo Expo **7**, 327–337 (2008).

[11] K. Pielichowska and K. Pielichowski, Progress in Materials Science **65**, 67–123 (2014).

[12] F. Agyenim, N. Hewitt, P. Eames, and M. Smyth, Renewable and Sustainable Energy Reviews **14**, 615–628 (2010).

[13] M. Longeon, A. Soupart, J.-F. Fourmigué, A. Bruch, and P. Marty, Applied Energy **112**, 175–184 (2013).

[14] Y. Wang, L. Wang, N. Xie, X. Lin, and H. Chen, International Journal of Heat and Mass Transfer **99**, 770–781 (2016).

[15] F. Fornarelli, S. Camporeale, B. Fortunato, M. Torresi, P. Oresta, L. Magliocchetti, A. Miliozzi, and G. Santo, Applied Energy **164**, 711–722 (2016).

[16] S. Almsater, W. Saman, and F. Bruno, AIP Conference Proceedings **1850**, p. 080001 (2017).

[17] F. Fornarelli, M. Valenzano, B. Fortunato, S. Camporeale, M. Torresi, and P. Oresta, Energy Procedia **148**, 471–478 (2018).

[18] F. Fornarelli, V. Ceglie, B. Fortunato, S. Camporeale, M. Torresi, P. Oresta, and A. Miliozzi, Energy Procedia **126**, 501–508 (2017).

[19] F. Fornarelli, S. Camporeale, and B. Fortunato, Applied Thermal Engineering 51–57 (2019).

[20] A. Miliozzi, G. Giannuzzi, and R. Liberatore, "Experimental and numerical analysis of the thermodynamic behaviour of simple latent heat thermal energy storage devices (in italian) *energia elettrica da fonte solare solare termodinamico (progetto b.1.3)*," Tech. Rep. Rds/Par2014/116 (ENEA, 2015).

[21] R. Mehrabian, M. Keane, and M. Flemings, Metallurgical Transactions **1**, 3238–3241 (1970).

[22] R. Mehrabian, M. Keane, and M. Flemings, Metallurgical and Materials Transactions **1**, 1209–1220 (1970).

[23] W. Bennon and F. Incropera, International Journal of Heat and Mass Transfer **30**, 2161–2170 (1987).

[24] V. Voller, M. Cross, and N. Markatos, International Journal for Numerical Methods in Engineering **24**, 271–284 (1987).

[25] V. Voller and C. Prakash, International Journal of Heat and Mass Transfer **30**, 1709–1719 (1987).

[26] W. Minkowycz, *Advances In Numerical Heat Transfer*, Advances in numerical heat transfer, Vol. 1 (Taylor & Francis, 1996) Chap. 9,, pp. 341–380.

[27] A. Brent, V. Voller, and K. Reid, Numerical Heat Transfer **13**, 297–318 (1988).